Sensors & Actuators: A. Physical 367 (2024) 114989

Contents lists available at ScienceDirect

Sensors and Actuators: A. Physical

journal homepage: www.journals.elsevier.com/sensors-and-actuators-a-physical

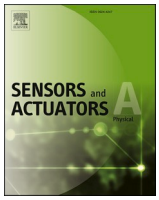

A smart idea to reject motion artefacts from ECG measurements due to sensor-body impedance

Anubha Manju Kalra [a,*], Gautam Anand [b], Andrew Lowe [c], Ray Simpkin [d], David Budgett [e]

[a] Department of Electrical Engineering, Auckland University of Technology, Auckland, New Zealand
[b] Institute of Biomedical Technologies, Auckland University of Technology, Auckland, New Zealand
[c] Department of Mechanical Engineering, Auckland University of Technology, Auckland, New Zealand
[d] Emrod Limited, Auckland, New Zealand
[e] Auckland Bioengineering Institute, The University of Auckland, Auckland, New Zealand

ARTICLE INFO

Keywords:
Electrocardiogram
Non-contact
Air-gap capacitance
Mathematical modelling
Charge amplifier
Tissue impedance

ABSTRACT

Electrocardiogram (ECG) records the electrical activity of the heart and is the most significant diagnostic indicator of health. The electrical activity propagates towards the skin and is typically measured using gel silver/silver chloride (Ag/AgCl) electrodes. The quality of the measured signal depends on the amplitude of the electrical activity, the conductivity of the tissues and skin, and that of the measuring electrode. Gel electrodes can cause skin irritability and are not suitable for long-term measurements requiring the diagnosis of paroxysmal arrhythmias. Dry electrodes are comparatively comfortable to wear but are highly dependent on body hair, sweating, and movement. Non-contact electrodes on the other hand avoid ohmic contact with the skin by providing a capacitive coupling between the skin and the electrode. They can be easily worn over clothing or can be measured from a distance. However, motion artefact remains the biggest challenge in such systems. This study proposes a novel two-channel circuitry for ECG acquisition along with a mathematical model to mitigate the effect of changing sensor-electrode capacitance in non-contact sensors. This method was modeled and validated at different sensor-electrode positions or air-gaps. The effect of change in mutual and parasitic capacitance between the sensor's channels, body tissue impedance, and the ratio of the areas of the two channels was also analysed in terms of Signal to Noise Ratio (SNR). The highest SNRs were achieved with smaller air-gaps and higher ratios of channels' areas.

1. Introduction

Electrocardiography (ECG) occurs due to polarization and depolarization of the heart due to the filling and emptying of the heart chambers and is used to assess heart rate, interbeat interval, wave shape, and heart rate variability. It is widely used in clinical practice, for example, to diagnose coronary artery disease or the cause of chest pain during a stress test, while the patient is running on a treadmill. Ambulatory ECG monitoring is used for the long-term recording of ECG signals, while the patient carries out his/her daily activities. Artefacts in ECG are caused by the patient's movement, moving cables, interference from outside sources, electromyography (EMG) interference, and electrical contact from elsewhere on the body. Most of these artefacts can be minimized by using proper electrode design and ECG circuitry. However, artefacts due to the subject's movement are hard to identify and eliminate and can be easily mistaken for symptoms of arrhythmia and the physiological effects of exercise, leading to misdiagnosis and false alarms.

Traditional adhesive sensor electrodes provide a stable, low-impedance signal source that allows for the low noise measurement of ECG signals, but the wires and adhesives are a considerable inconvenience and discomfort to the user, thereby causing longer-term personal health monitoring with these traditional devices untenable [1–4]. Several studies have reported the use of dry and capacitive sensors for ECG measurements. However, motion artefact remains to be a major challenge in most of these studies. In one study, contactless capacitive electrodes were developed to exclusively amplify differential biopotentials [5]. However, the study overlooked the potential consequences of amplifying signals resulting from movements such as body tremors, muscle contractions, or patient repositioning. Another investigation compared various technologies for ECG monitoring,

* Corresponding author.
E-mail address: anubha.kalra@aut.ac.nz (A.M. Kalra).

https://doi.org/10.1016/j.sna.2023.114989
Received 26 June 2023; Received in revised form 28 November 2023; Accepted 28 December 2023
Available online 14 January 2024

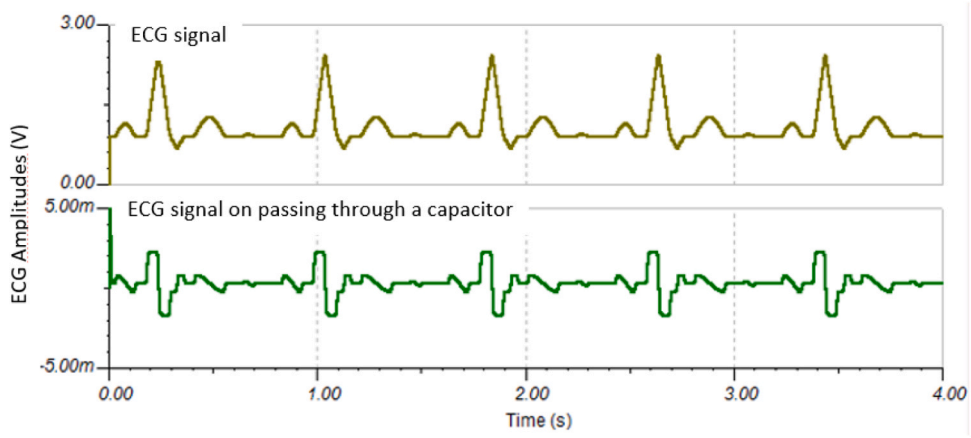

Fig. 1. Artificial ECG (in yellow) and differentiation of ECG after passing through a capacitor (in green). (For interpretation of the references to color in this figure legend, the reader is referred to the web version of this article.)

highlighting challenges in signal accuracy due to motion when utilizing capacitive sensing [6]. In a separate research project, an optimized design for non-contact ECG recording was crafted, tailored specifically for capturing small-amplitude ECGs in rats [7]. It is important to note that motion was restricted by confining the rat within a cage.

Some techniques to track and eliminate motion artefact involve the use of accelerometers [8–10], differential transformers [11], gradiometers [12], or optical sensors [13]. However, these devices have only been shown to remove baseline wander noise and are often coupled with software filters that could remove important diagnostic information from ECG signals [8,14–17]. Moreover, it is difficult to remove motion artefact that has similar amplitude, frequency, and morphology to ECG with software filtering. Noise removal techniques applied to mitigate these artefacts can only improve the signal quality to some extent and do not work in cases of extreme motion such as running or jumping.

An improvement in the ECG signal quality was observed by introducing foam padding to the electrode design [18], however, the signal showed high susceptibility to motion at very high electrode-skin contact pressures [19]. One of the recent works [20] proposed a new electrode design to collect a reference signal from an electrode placed beside the main electrode for ECG measurement. The study made an unverified presumption that ECGs are smaller in amplitude than motion signals.

In this study, we propose a novel non-contact ECG sensor technology that can be used for long-term monitoring and efficiently reject/eliminate motion artefacts without the need for hard filtering or signal smoothening. Integrating these sensors into emergency medical equipment, examination tables, beds or other furniture is an attractive option. A patent application was filed for this technology in May 2020 and full approval was granted in June 2022 (Title – A biopotential sensor, device and process, Publication number 20220202336) [21]. Section II shows a simulation of the ECG signal at different sensor-electrode distances to understand the effect of change in the signal's shape due to varying air-gap capacitances. An electronic circuit was developed to retain the shape of the original signal, and results were validated via a benchtop setup. Section III describes the mathematical model relating the biological tissue (skin and fat), and the sensor/electrode. The novel technique of signal reconstruction by rejecting the effect of motion/skin-electrode impedance using a two-channel electronic circuit and a set of mathematical equations has been discussed in detail while considering the effect of mutual and parasitic capacitances, longitudinal and cross-tissue impedances, and change in electrodes' areas.

2. Sensor design

2.1. Simulation

Human skin can be modelled as a parallel Resistance-Capacitance (R || C) circuit. The ECG signal on the skin's surface depends on the size of the skin's pores, rate of perspiration, and impedance of blood, muscle, fat, and skin. Gel electrodes work by inducing the electrolyte gel in the pores of the skin and thereby shunting the epidermal cell membrane impedance. In dry sensing, the electrode surface is conductive (more

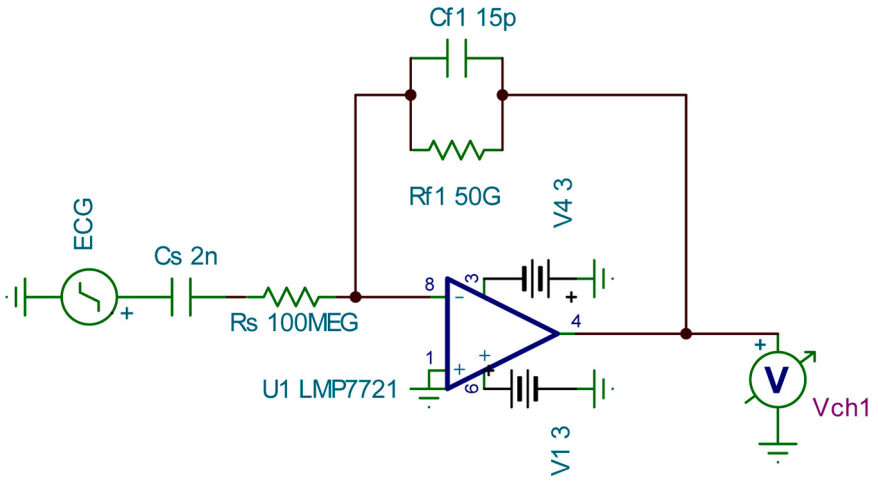

Fig. 2. Charge amplifier.

Table 1
Range of circuit parameters of the charge amplifier.

Circuit parameters	Desirable Range
Cs	22 pF-2nF
Rs	50Meg-100Meg
Rf	10 G-50 G
Cf	15 pF-22 pF

resistive than capacitive) and in direct contact with the skin without an air-gap: the gap between the skin and the sensor). The presence of sweat reduces the impedance of the stratum corneum to much extent. Assuming V_{ecg} as the signal that passes through an air gap with capacitance C_{air} has sensed as displacement current i_d over a time t, as seen in Eq. 1.

$$i_d = C_{air}\frac{dV_{ecg}}{dt} \tag{1}$$

According to Eq. 1, as the air gap from the sensing site is increased, capacitance C_{air} decreases, and the ECG signal gets differentiated and attenuated. An artificial ECG signal with a primary frequency of 1 Hz was created using MATLAB and fed through a capacitor to observe the differentiation effect (Fig. 1). Air acts as a capacitor with a low dielectric constant$\in_0 = 1$.

To trump the effect of signal differentiation and restore the ECG wave shape, a circuit (Fig. 2) with a charge amplifier was designed in TINA-TI (TEXAS instruments) software with input as ECG from Fig. 1.

C_s is the series capacitance offered by the air-gap, *and* R_s, R_f, C_f, *and*V_{ch1} are the series resistance, feedback resistance, feedback capacitance, and voltage output of the charge amplifier, respectively.

Signal restoration and integration are possible if Eq. 2 is satisfied.

$$R_f \times C_f > R_s \times C_f \tag{2}$$

The corner frequencies f_a&f_b are shown in Eqs. 3 and 4.

$$f_a = \frac{1}{2.pi.R_f.C_f} \tag{3}$$

$$f_b = \frac{1}{2.pi.R_s.C_f} \tag{4}$$

In cases where there is no series resistance in the circuit, there is only one corner frequency (lower cut-off f_a).

ECG frequency range is between 0.5 Hz to 150 Hz. Only those features lying within the range of the corner frequencies will be integrated. Opamp LMP7721MA was used in the circuit due to its ultra-low input bias current characteristics. Chosen for its low-input bias current, impressive Gain Band Width (GBW) of 17 MHz, and a high open-loop gain of 120 dB facilitating precise signal conditioning, this amplifier functions within a supply voltage range of 1.8 V to 5.5 V. A range of passive components was selected keeping in mind the noise minimization, better signal acquisition, filter's cut-off values, and providing sufficient gain without saturating the signal, as seen in Table 1.

2.2. Printed circuit board design

After finalizing the charge amplifier's parameters, the design was sketched in Altium Designer system engineering software (PCB design and software tool, Australia) as seen in Fig. 3 and the Printed Circuit

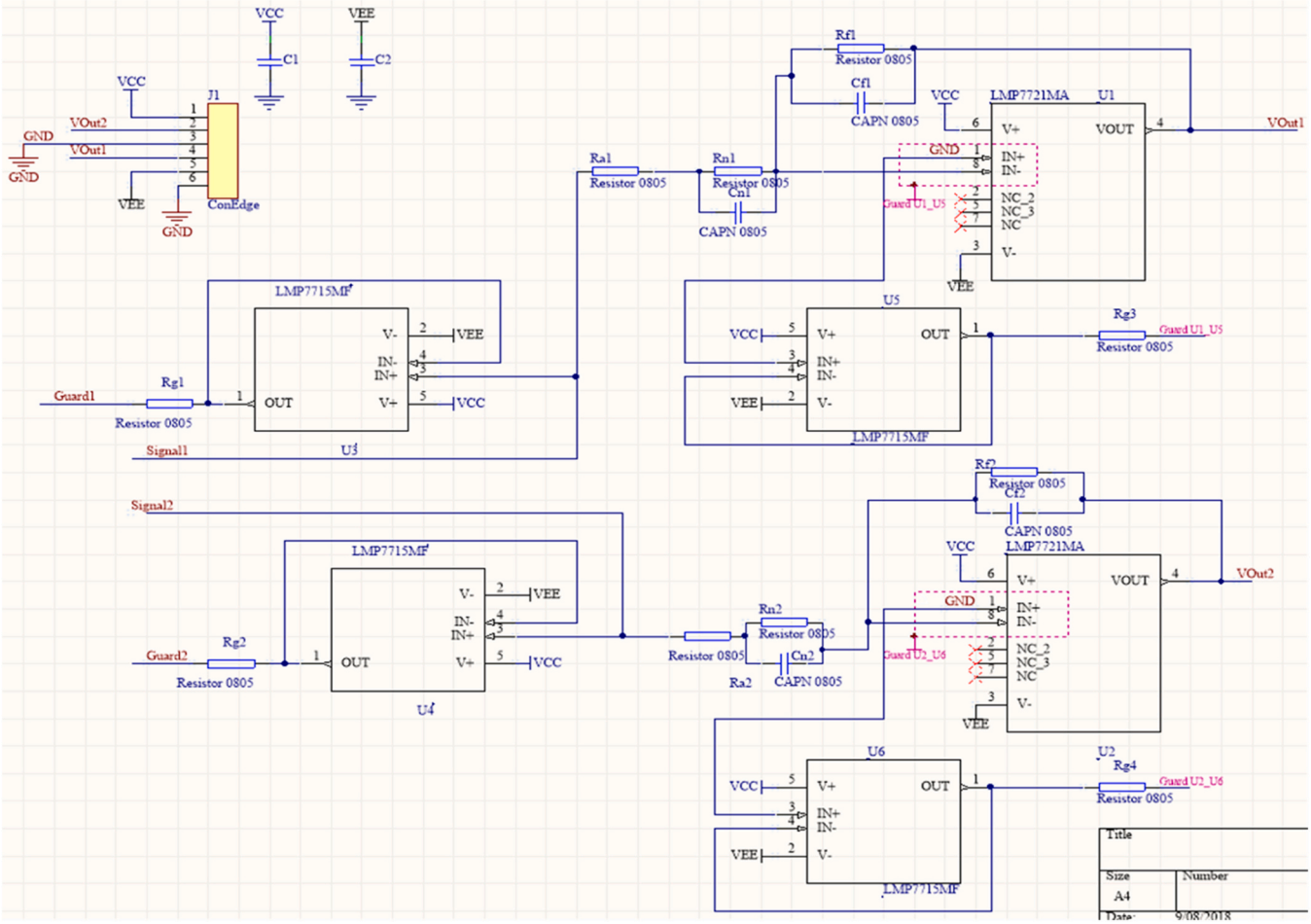

Fig. 3. a: Sketch of the charge-amp circuit with guarding in Altium software. b: PCB design view of the charge amplifier circuit.

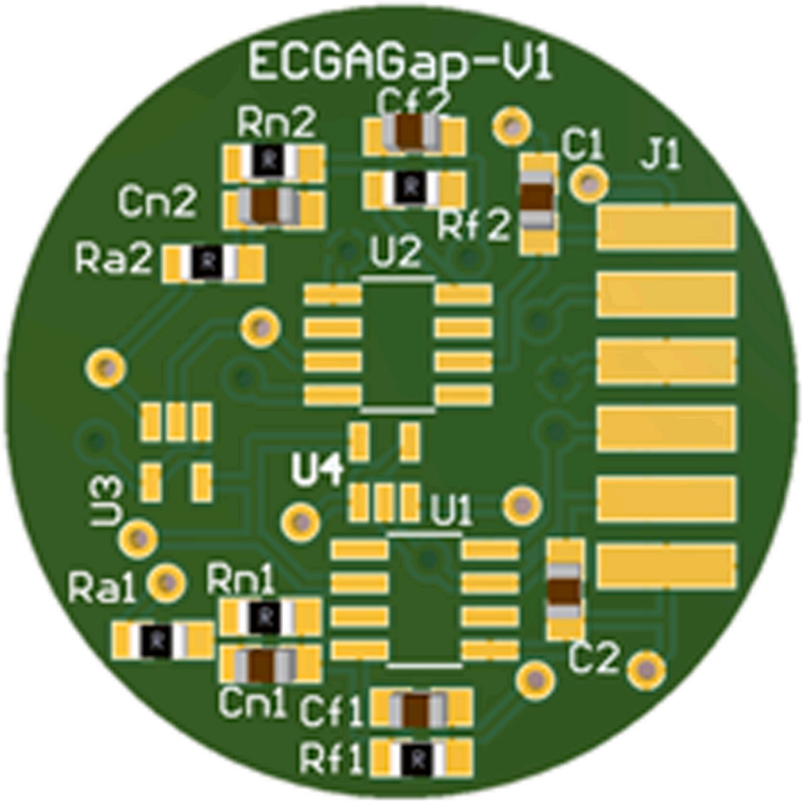

Fig. 3. (*continued*).

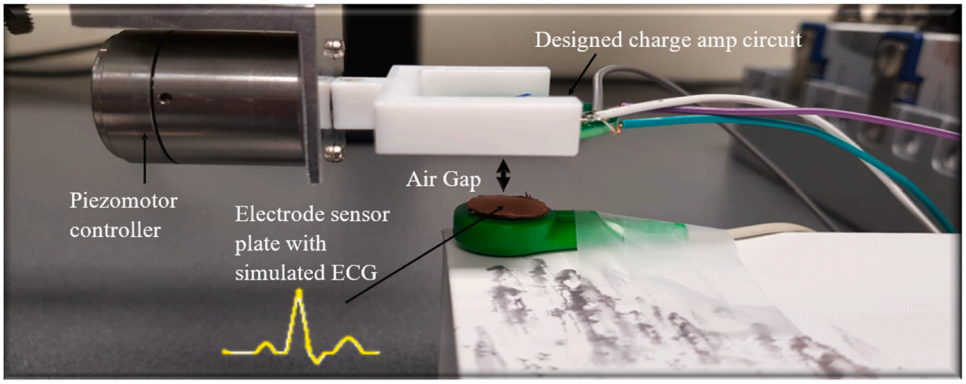

Fig. 4. Experimental set-up showing charge amp PCB clamped to Piezomotor.

Board was sent for manufacturing. A guarding circuit ($Guard_1 and Guard_2$)was implemented using the OpAmp LMP7715, to prevent and minimize errors due to leakage currents (Fig. 3a and b). The design used two channels to ensure repeatable outputs under the same loading conditions. The outputs from V_{out1} and V_{out2} should be consistent and repeatable with respect to inputs from $Signal_1 and Signal_2$.

2.3. Results from experimental validation

An artificially created ECG signal (0.1 V in magnitude) was given to the electrode sensor plate using a signal generator (Tektronix AFG3102C, Oregon, United States). Air gap motion was controlled using a micrometer piezo motor (Piezo legs LT20, Piezomotor, Sweden). The designed charge amplifier PCB was clamped to the motor which was displaced at different air-gaps (Fig. 4).

The input signal's shape changed (as seen in Fig. 1) due to air-gap capacitance. The shape was restored after passing the signal through the charge amplifier of the PCB (V_{out}), but a variation in signal amplitudes was observed as the air-gap was altered. In Fig. 5, *d* represents the change in distance (in mm). A very slight change in ECG's amplitudes is observed when the air gap was between 0 mm and 0.2 mm. The designed sensor was capable of sensing ECG signals in real conditions from distances up to 20 mm. Practically, a reduction in the sensor-body gap can be possible by using padding to secure the sensor in place.

The next sections entail the use of a novel air-gap rejection model to restore both the shape and amplitude of the ECG signal at different air-gaps and conditions.

3. Novel ECG air-gap rejection model

In capacitive ECG measurements employing textile/fabric sensing, it has been observed that the signal coupling is mainly dominated by the

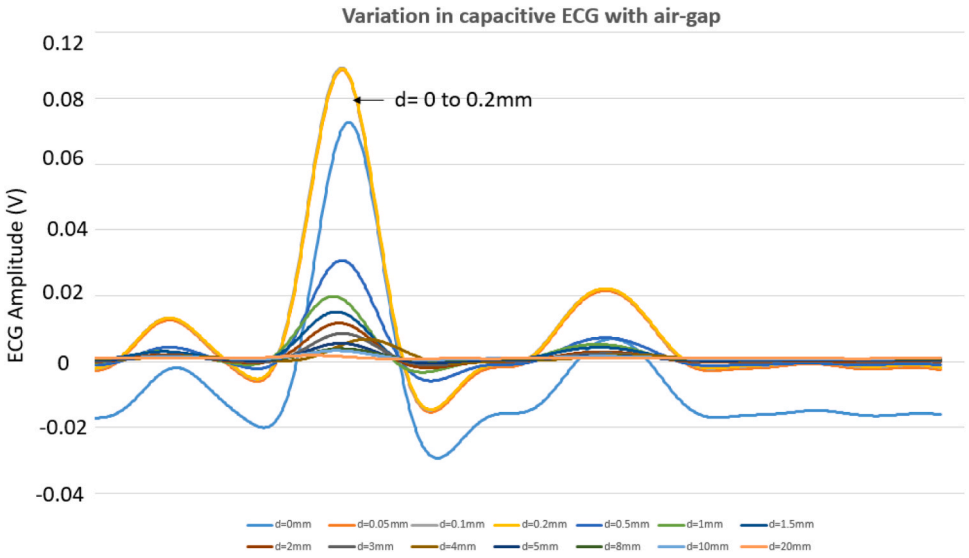

Fig. 5. Variation of ECG amplitudes with changing air-gaps.

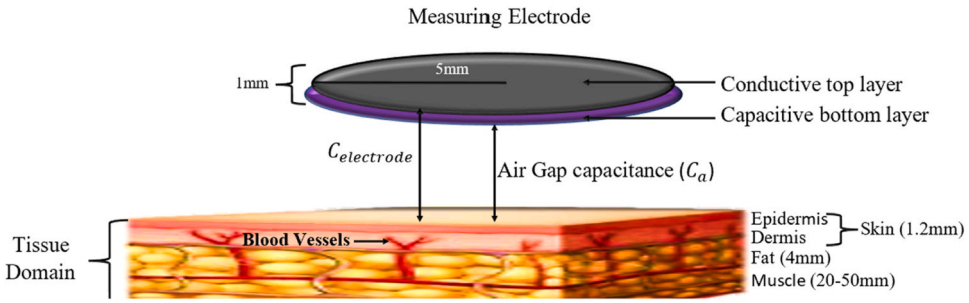

Fig. 6. Tissue membrane with the non-contact measuring electrode.

resistive part of the electrodes causing large voltage noise at lower frequencies of interest. Whereas in several cases, the dry contact sensors are more capacitively than resistively dominated than non-contact sensors [22,23].

Thus, introducing an intentional air-gap can actually mitigate these problems by making the skin-electrode interface purely capacitive. The intrinsic structure of any biological tissue defines its electrical properties such as conductance and admittance. As mentioned earlier, the electrical properties of tissue are subject to change to its thickness, age, gender, sweat, and environmental conditions such as humidity and temperature.

This section will first propose a model for a skin-electrode interface considering the resistances and capacitances of the non-contact electrode, epidermis, dermis, and fat. A transfer function of the above model will be analysed to account for the combined effect of all the layers of the tissues. The rest of the section will introduce a novel method to reject the effect of air-gap capacitance and the collective impedance offered by tissues for the action potential to reach the top of the skin's surface.

3.1. Mathematical and electrical modelling of biological tissue and non-contact electrode

A diagram representing the collective model of the tissue membrane with the non-contact electrode can be seen in Fig. 6.

The impedance of biological tissue can be analysed in terms of resistance and capacitance ignoring the inductive effects. Typically, the impedance of biological tissues is represented by the Cole-Cole equation:

$$Z(\omega) = R_\infty + \frac{R_o - R_\infty}{1 + (j\omega\tau)^\alpha} \tag{5}$$

Where R_∞, R_0, τ, and α are the Cole parameters defining the overall impedance spectrum. The tissue behaves like a conductor for low frequencies, but the capacitive effects become more pronounced at higher frequencies. This type of variation in the distribution of tissue properties into resistive and capacitive is known as dispersion. The lag between the conduction and the displacement electric fields is identified through a relaxation time or time constant τ, where α is the coefficient of relaxation in the Cole-Cole equation and is dependent on the nature of the material. α depends on the property of the tissue layer and lies between 0 and 1. R_∞ is the resistance measured at very high frequencies, whereas R_o is the resistance at low frequencies. The action potential from the heart propagates as a spatially dynamic electric field gradient across various tissue domains. Muscle, blood, and bone show high conductivities and are highly perfused, whereas skin and fat are less conductive and poorly perfused. In this study, ECG is represented by an electric potential V_{ecg} due to the dipole moment Φ_{DL} subtended by each layer L at an angle θ, where,

$$V_{ecg} = \Phi_{DL}.\theta \tag{6}$$

Since the signal of interest (ECG) lies in the lower frequency range (0.1–150 Hz), Eq. 7 can be simplified as:

$$Z(\omega) = \frac{R_o}{1 + (j\omega\tau)^\alpha} \tag{7}$$

Table 2
Conductivity, permittivity, and thicknesses of tissue layers.

Tissue	Relative Permittivity($\in_r$)	Measurement frequency (Hz)	Conductivity at DC (σ) (S/m)	Thickness (t) (mm)
Blood	3×10^3	1000	0.43-0.7	-
Muscle	1.5×10^6	10	0.3-0.8	20-50
Bone	3×10^6	10	0.5	2
Fat	10^7	10	0.02-0.04	4
Dermis	3700	10	0.0000125	1
Epidermis	10,000	2	0.00002	0.2

A summary of conductivities and permittivity of tissues in the lower frequency range and their thicknesses are given in Table 2.

The electric field in skin and fat layers is relatively low and V_{ecg} is divided in these tissues depending upon their resistances and capacitances. An equivalent circuit considering V_{ecg} passing through fat, skin, and air gap to the measurement channel can be seen in Fig. 7.

Based on the non-contact electrode dimensions (with radius r = 5 mm) in Fig. 5 and permittivity and conductivity values in Table 2, the resistances and capacitances of fat and skin are:

$$R_{fat} = \frac{t_{fat}}{\pi(r)^2 \times \sigma_{fat}} = 1.7k\Omega, R_{skin} = \frac{t_{skin}}{\pi(r)^2 \times \sigma_{skin}} = 76.4k\Omega, C_{fat} = \frac{\pi(r)^2 \in_0 \in_{rfat}}{t_{fat}} = 1.6\mu F, C_{skin} = \frac{\pi(r)^2 \in_0 \in_{rskin}}{t_{skin}} = 1.5nF(where \quad \in_{rskin} = \frac{\in_{r\_dermis} \times \in_{r\_epidermis}}{\in_{r\_dermis} + \in_{r\_epidermis}} = 2700)$$

In Fig. 7, the non-contact electrode has a dielectric cotton layer at the bottom and a conductive metal on top. C_{air} is calculated at a gap of 1 mm and the measurement circuit is the same as in section II (Sensor Design).

Transfer function analysis of the system is done to relate the input signal with the system's response through the following set of equations in Laplacian transform.

$$Z_f = \frac{R_f}{1 + sR_fC_f} \tag{8}$$

$$Z_s = \frac{1 + sR_sC_s}{sC_s} \tag{9}$$

$$Z_e = \frac{R_{dry}}{1 + sR_{dry}C_{dry}} + \frac{R_{cotton}}{1 + sR_{cotton}C_{cotton}} \tag{10}$$

$$Z_a = \frac{1}{sC_{air}} \tag{11}$$

$$\text{Transverse Impedance} \rightarrow Z_T = \frac{R_{fat}}{1 + sR_{fat}C_{fat}} + \frac{R_{skin}}{1 + sR_{skin}C_{skn}} \tag{12}$$

$$V_{ch1}(s) = -\frac{Z_f}{Z_s + Z_e + Z_a + Z_T} \quad V_{ECG}(s) \tag{13}$$

$$V_{ch1}(s) = -\frac{\left(\frac{R_f}{1+sR_fC_f}\right).V_{ECG}(s)}{\left(\frac{1+sR_sC_s}{sC_s} + \frac{R_{dry}}{1+sR_{dry}C_{dry}} + \frac{R_{cotton}}{1+sR_{cotton}C_{cotton}} + \frac{1}{sC_{air}} + \frac{R_{fat}}{1+sR_{fat}C_{fat}} + \frac{R_{skin}}{1+sR_{skin}C_{skn}}\right)} \tag{14}$$

3.2. Air-gap cancellation technique

In this section, a novel technique to remove the effect of air-gap capacitance from the measured ECG will be introduced.

The non-contact electrodes can be designed in a way to introduce two different capacitances such that the ratio of their capacitances is known (see Fig. 8).

The ratio of electrode, skin, and air-gap impedances for two electrodes is the same as the ratio of their areas $n = 2$

$$\frac{Z_{T1}}{Z_{T2}} = \frac{Z_{e1}}{Z_{e2}} = \frac{Z_{a1}}{Z_{a2}} = \frac{Area \quad of \quad electrode2}{Area \quad of \quad electrode1} = n = 2$$

The channel's output for the second electrode can be expressed as:

$$V_{ch2}(s) = -\frac{Z_f}{Z_s + \frac{Z_e + Z_a + Z_T}{n}} \quad V_{ECG}(s) \tag{15}$$

$$V_{ch2}(s) = -\frac{\left(\frac{R_f}{1+sR_fC_f}\right).V_{ECG}(s)}{\left(\frac{1+sR_sC_s}{sC_s} + \frac{\frac{R_{dry}}{1+sR_{dry}C_{dry}} + \frac{R_{cotton}}{1+sR_{cotton}C_{cotton}} + \frac{1}{sC_{air}} + \frac{R_{fat}}{1+sR_{fat}C_{fat}} + \frac{R_{skin}}{1+sR_{skin}C_{skn}}}{n}\right)} \tag{16}$$

From Eqs. 14 and 16, the unknown impedance can be eliminated, and the original ECG can be reconstructed (see Appendix A) in the frequency domain as:

$$V_{ECG}(s) = \frac{V_{ch1}(s) \times V_{ch2}(s)}{(V_{ch2}(s) - nV_{ch1}(s)} \times \frac{(n-1)(1 + sR_sC_s)(1 + sR_fC_f)}{sC_sR_f} \tag{17}$$

As seen from Eq. 17, the ECG signal can be extracted by using outputs

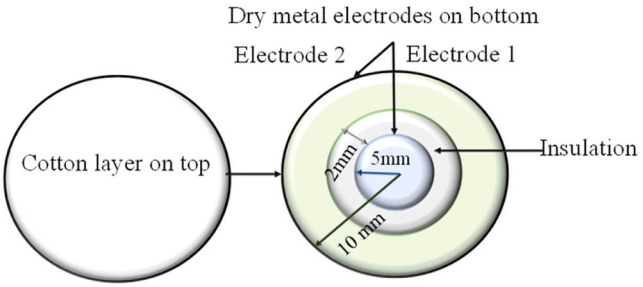

Fig. 8. Proposed electrode design to cancel air-gap capacitance.

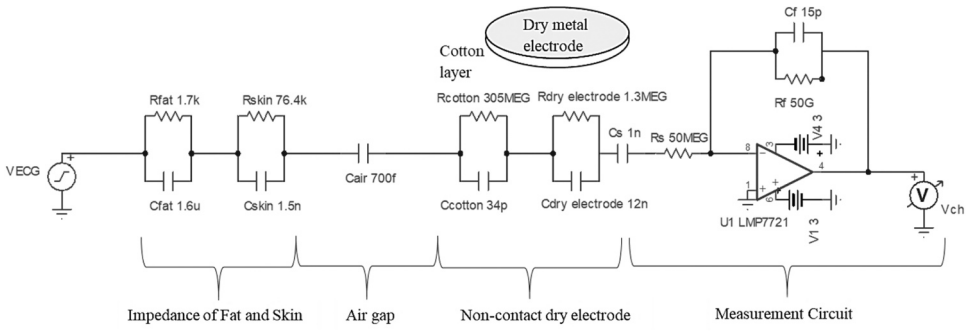

Fig. 7. Combined electrical model considering impedance of fat, tissue, and air gap.

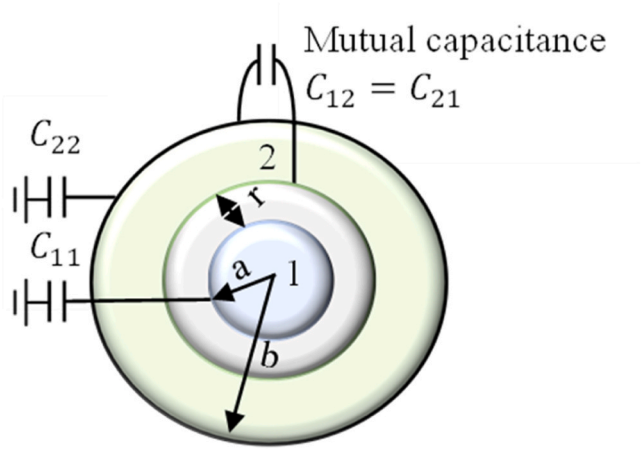

Fig. 9. Maxwell capacitance between two conductors.

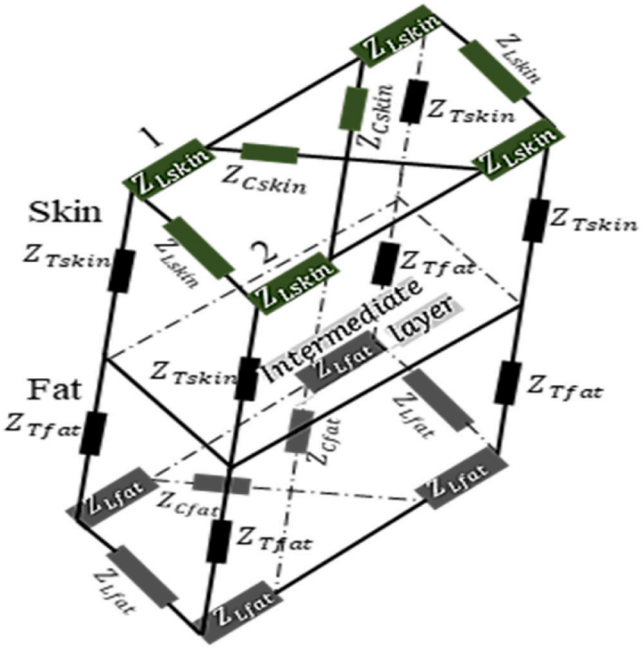

Fig. 10. Three-dimensional model of fat and skin with transverse Z_T, longitudinal Z_L, and cross impedance Z_C.

and parametric component values from each channel (see Appendix C). The next section will discuss the effect of mutual impedance between the two concentric electrodes considered in this study.

1. Effect of mutual and parasitic impedance between channels

A Maxwell capacitance matrix C_maxwell provides a relation between voltages on a set of conductors to charges on the conductors. The mutual and auto capacitances between two sets of conductors can be represented in Fig. 9.

For a system with two sensors, placed r mm apart, where r = 2 mm from Fig. 9, their auto (C_{11} and C_{22}) and mutual (C_{12}*and*C_{21})capacitances can be calculated as

$$C_{maxwell} = \begin{bmatrix} C_{11} & C_{12} \\ C_{21} & C_{22} \end{bmatrix} \tag{18}$$

The mutual capacitance between the electrodes can be calculated as [24].

$$C_{12} = \frac{2\pi\varepsilon_0 L}{\ln\frac{a}{b}} = C_{21} = 0.016pF \tag{19}$$

where L= 0.02 mm is the thickness of the solder mask in a PCB (or metal electrode). In further section, the impact of parasitic capacitance on the reconstructed ECG's quality will be studied.

2. Effect of fat and skin's longitudinal and cross impedance

The impedance of fat and skin can be modelled as a parallel RC circuit, where only transverse impedance Z_T between the layers is considered. However, when another channel V_{ch2} is added to the measurement circuit, it is also important to consider the effects of longitudinal (Z_L) and cross impedances (Z_C) between the tissue layers. A three-dimensional model of the fat and skin can be depicted in Fig. 10.

The transverse impedances of the tissues are inversely related to their thickness, whereas the longitudinal and cross impedances on the tissue's surface depend on their surface resistivity and other factors such as level of hydration, age, gender, hair, etc. Both Z_L and Z_C are a function of the distance between electrodes 1 and 2 and can be assumed as purely resistive instead of parallel RC as the displacement currents on the surface are much lower than their conduction currents. Surface resistivity is measured using concentric electrodes based on assumption that all current flows between the electrodes on the surface and does not penetrate the deep layers. Since V_{ECG} is taken as a point voltage, we will only consider Z_L and not Z_C here.

Resistances of skin and fat can be evaluated as a function of the radii of the inner electrode and the distance between them (r from Fig. 9) from the following equation, where surface resistivities of skin and fat at lower values are approximately 10^7 and 10^4 respectively.

$$R_{L-skin} = \frac{\rho_{skin}}{2\pi}\ln\left(\frac{Radius_{inner\quad electrode}}{Radius_{inner\quad electrode} + r}\right) \tag{20}$$

$$R_{L-fat} = \frac{\rho_{fat}}{2\pi}\ln\left(\frac{Radius_{inner\quad electrode}}{Radius_{inner\quad electrode} + r}\right) \tag{21}$$

The effect of change in Z_L due to change in electrodes' gap on ECG reconstruction is shown in further sections.

3. Effect of change in area ratio

The effect of changing the area's ratio 'n' (from 2 to 10) was observed. The tolerance to ± 20% deviation in n was also tested keeping in mind that the effective area ratios can differ in practicality. The stability and gain of the transfer function at various ratios of series resistances and capacitances of the channels can be evaluated to optimize the ECG reconstruction. The current transfer (T.Fn) is defined by Eq. 22 (see Appendix A).

$$T.Fn = \frac{(n-1)(1+sR_sC_s)(1+sR_fC_f)}{sC_sR_f} = \frac{s^2\left(nR_sC_sR_fC_f - R_sC_sR_fC_f\right) + s\left(nR_sC_s + nR_fC_f - R_sC_s - R_fC_f\right) + n - 1}{sC_sR_f} \tag{22}$$

where R_{s1}, R_{s2}, and C_{s1}, $C_{s2}$are series resistances and capacitances of the first and second channel respectively. If we take separate feedback values R_f*and*C_f for two channels, then ECG reconstruction using transfer function analysis will not be possible. Therefore, R_f*and*C_f for both channels are taken to be the same in this study.

Considering the ratios $\frac{R_{s2}}{R_{s1}} = m$, $\frac{Area\ of\ electrode2}{Area\ of\ electrode1} = n$, $\frac{C_{s1}}{C_{s2}} = k$, the following four cases can be implemented.

Case 1: $m, n,$ *and* k *are independent of one another* (NON-CAUSAL).

As shown in Eq. 22, the system will be non-causal, showing a

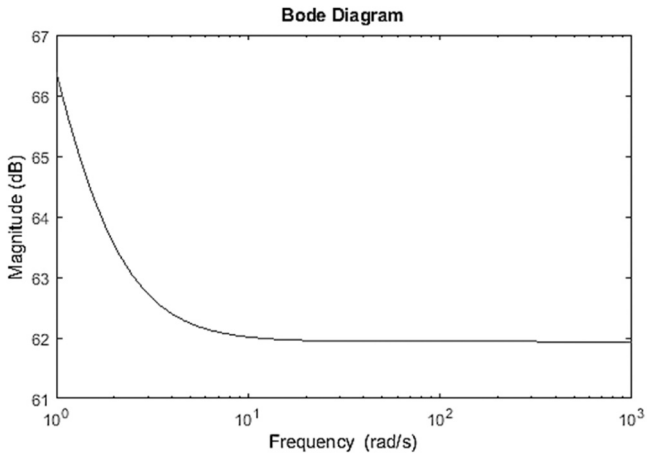

Fig. 11. Bode plot for T.Fn2 where number of poles=number of zeros.

dependence on input values from the future if $m, n,$ *and* k are not related to each other.

Case 2: $m = n$ *and* k *is not equal to* m *and* n (CAUSAL).

In this case, the transfer function equation becomes T.Fn2 as seen in Eq. 23 (see Appendix B).

$$T.Fn2 = \frac{s\left(nR_fC_fC_{s2} - C_{s1}R_fC_f\right) + nC_{s2} - C_{s1}}{sC_{s1}C_{s2}R_f} \tag{23}$$

The above system is a causal system where the outputs depend on the past and current inputs but not future inputs. The frequency response of this system can be seen in Fig. 11.

Case 3: $m = k$ *and* n *is not equal to* m *and* k (NON-CAUSAL).

The system will be non-causal as seen from Eq. 22.

Case 4: $n = k$ *and* m *is independent of* n *and* k (NON-CAUSAL).

The transfer function will become a first-order equation, but the system will be non-causal as the number of zeros> the number of poles (see Eq. 24).

$$T.Fn3 = \frac{s\left(nR_fC_fR_{s1} - R_{s2}R_fC_f\right) + nR_{s1} - R_{s2}}{R_f} \tag{24}$$

Case 5: $m = n = k$ (TRANSFER FUNCTION = 0, THEREFORE RECONSTRUCTION NOT POSSIBLE).

The transfer function, in this case, will be zero and therefore ECG cannot be reconstructed.

The section below demonstrates the change in reconstructed ECG as a function of all parameters in section III (b).

3.3. Results from experimental validation

This section is based on a modified PCB design with a matrix configuration of the two-channel system. It has been assumed that the input voltages to the 2 channels are similar (ECGs) due to a very small gap between them, as seen in Fig. 12.

Simulated ECG was fed from the signal generator V_{ECG} ((Tektronix AFG3102C, Oregon, United States), at five different air-gaps (1 mm, 2 mm, 3 mm, 4 mm, and 5 mm). This range was chosen keeping in mind the motion or displacement that can occur between the skin-electrode surface while performing day-to-day activities. Two output signals were received and were reconstructed to retain the original signal. The final signal V_{REC} was reconstructed (see Fig. 13) from the two channels - V_{ch1} and V_{ch2}.

Table 3 compares the Signal Noise Ratios (SNR) of reconstructed ECGs with increasing air-gaps, where,

$$SNR = 10\log\left(\frac{V_{ECG}}{V_{ECG} - V_{REC}}\right)^2 \tag{23}$$

The reconstruction was smoother at smaller air-gaps, as seen in Table 3, and Fig. 14.

The relationship between inter-electrode distance and mutual capacitance and SNR at a 1 mm air-gap can be seen in Table 4.

The effect of adding Z_{Lfat} and Z_{Lskin} between two channels on ECG reconstruction was investigated. A small resistor in parallel with a capacitor was placed between the fat and skin layers of the two chan-

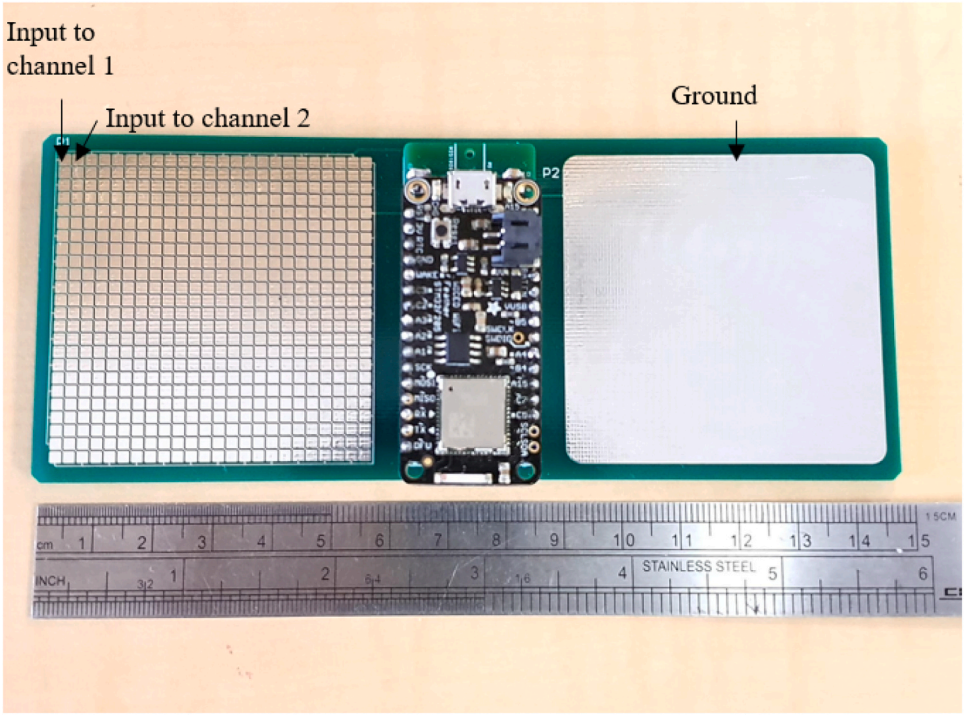

Fig. 12. Novel two-channel system to get ECG from the palms. The left side receives ECG signals while the right side is grounded.

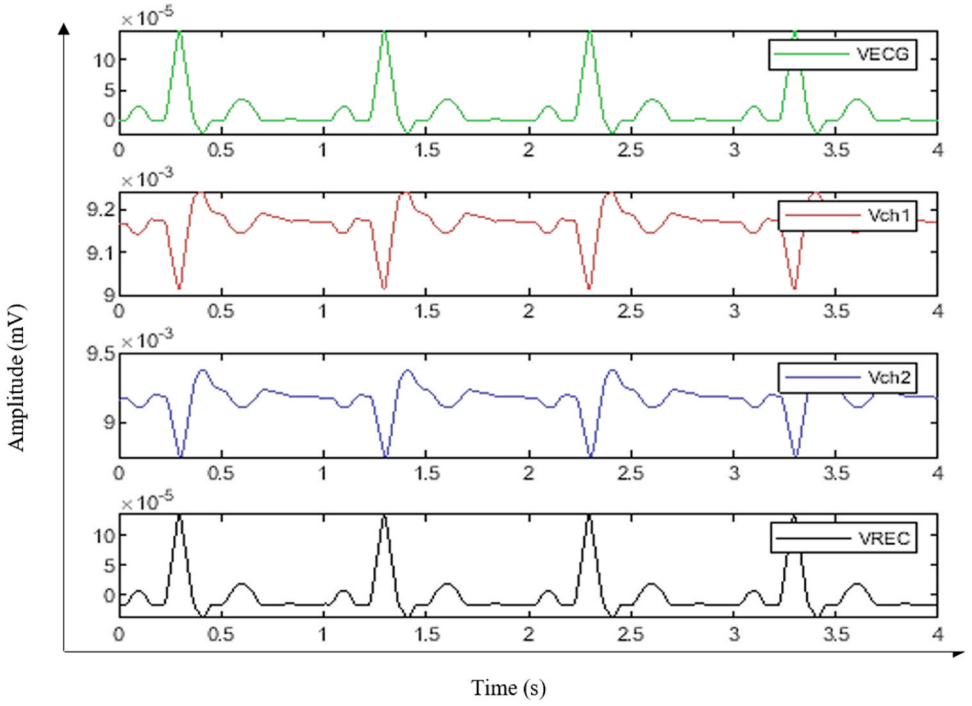

Fig. 13. Reconstruction of ECG by eliminating air-gap impedance.

Table 3
Comparison of SNRs of reconstructed ECGs at various air-gaps.

Air Gap (mm)	SNR (dB)
1	50.40
2	38.88
3	32.49
4	25.47
5	21.6

Table 4
Relationship between inter-electrode distance, and mutual capacitance between electrodes using Eq. 23.

Inter-electrode Distance (mm)	Mutual capacitance (pF)	SNR (dB)
1	0.019	48.28
2	0.016	49.405
3	0.014	49.87
4	0.012	49.93
5	0.011	50.01

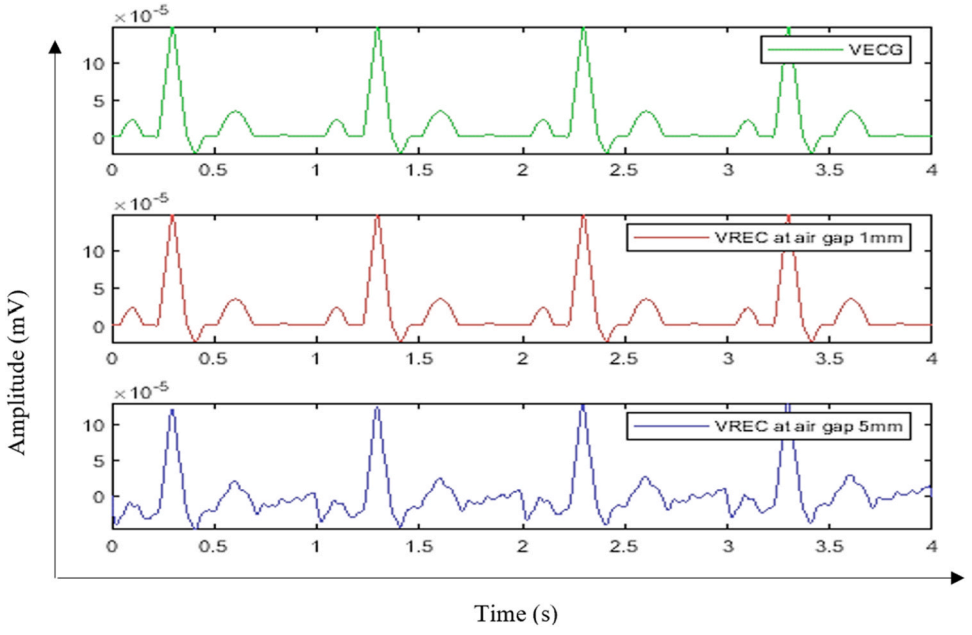

Fig. 14. Reconstructed ECG at 1 mm and 5 mm air gaps.

Table 5
Relationship between interelectrode distance and longitudinal impedances of fat and skin and SNRs.

Interelectrode distance (mm)	Z_L fat (Ω)	Z_L skin (Ω)	SNR (dB)
1	1.6	1.6k	50.40
2	3.1	3.1k	50.40
3	4.8	4.8k	49.89
4	6.3	6.3k	49.92
5	7.9	7.9k	49.39

nels. From Eqs. 20 and 21, it can be noted that the longitudinal resistances depend upon the inter-electrode distance (see Table 5).

Different combinations of ratios of electrode areas (n) were taken by changing the diameters. SNRs with ± 20% deviation at different values of n (from 2 to 10) were calculated (see Fig. 15).

The conclusions derived from the results are discussed in detail in the next section.

4. Discussion

In section II of the study, a simulation was carried out to show the change in shape due to air gaps. A PCB with a charge amplifier and a guarding circuit was designed and printed and circuit parameters were optimized to ensure low noise and high gain without saturating the output. The bench-top experiments conducted by changing the sensor-electrode distance showed that ECG was best reconstructed (in terms of amplitude and shape restoration) at air gaps of up to 0.2 mm. The maximum air-gap of 20 mm produced the maximum distortion in amplitude.

In section III, a mathematical model was developed to observe the effect of the overall body tissue impedance offered by fat and skin, and the electrode impedance due to a dry sensor and a cotton fabric. The values of the impedances were calculated using the Cole-Cole equation, and the existing values of permittivity and conductivities. The transfer function equations were calculated for the two channels of the PCB. The ECG was reconstructed from the transfer functions of the two channels, and the overall impedance offered by the biological tissues and the electrode was eliminated. This approach was verified via simulations and experiments. The SNRs of the reconstructed ECGs were significantly high (>20) for the air-gap ranges between 1–5 mm. However, Table 3 shows a significant reduction in SNR from 50.4 to 21.6 at air-gaps 1 and 5 mm, respectively. This indicates that the total effect of impedance on the channels is dissimilar at higher air-gaps (see Fig. 14).

In the next section, steps were taken to optimize the sensor design such as the distance between the two electrode channels to ensure minimum distortion due to the mutual and parasitic capacitance. Maxwell capacitance matrix was calculated, and the results indicate an increase in SNR and a reduction in mutual capacitance on increasing the inter-electrode gap (Table 4). The effect of adding Z_{Lfat} and Z_{Lskin} was also observed by using a set of parallel R and C combinational values at different inter-electrode separations. Since V_{ECG} is taken as a point voltage, we only considered the impact of longitudinal (Z_L) and not Z_C here. The SNRs were not affected by increasing the longitudinal tissue impedances. Table 5 reveals that the Signal-to-Noise Ratio (SNR) rises with a decrease in longitudinal impedances caused by fat and skin. Therefore, from a design standpoint, it is advisable to opt for a smaller inter-electrode distance.

The stability and gain of the transfer function at various ratios of series resistances and capacitances of the channels can be evaluated to optimize the ECG reconstruction. The values of feedback components were kept the same across both channels to ensure a causal system. Four cases with different relationships between the ratios of series resistances, areas, and capacitances between the two channels ('m′, 'n′, and 'k′ respectively) were considered. It was found that the ratio of the channels' series resistances and areas should be the same, and not equal to the ratio of their series capacitances for the system to be stable. A higher value of 'n′ ensured la better SNR and less sensitivity to changes (Fig. 15).

5. Conclusion

This study focuses on developing a non-contact sensor that can produce reliable, noise-free ECG signals that are unaffected by motion or displacement between the sensor and the body. A novel method using two-channel electronics was simulated and validated under different conditions. Sensor optimizations were performed by considering factors like biological tissue impedance, mutual and parasitic capacitances, and electrode areas. High-fidelity results were achieved and measured using a benchtop setup. The SNRs were highest at smaller air-gaps, larger interelectrode distances, and higher ratios of areas between the channels. For the system to work, and to ensure its stability, it was important to have the ratio of the channels' series resistances equal to the ratios of their areas and unequal to the ratio of their series capacitances. Currently, clinical trials using our novel sensor integrated into a vest are being performed (see Appendix D for pilot testing results). Future work will include deriving conclusions from those trials and optimizing the system's design and electronics.

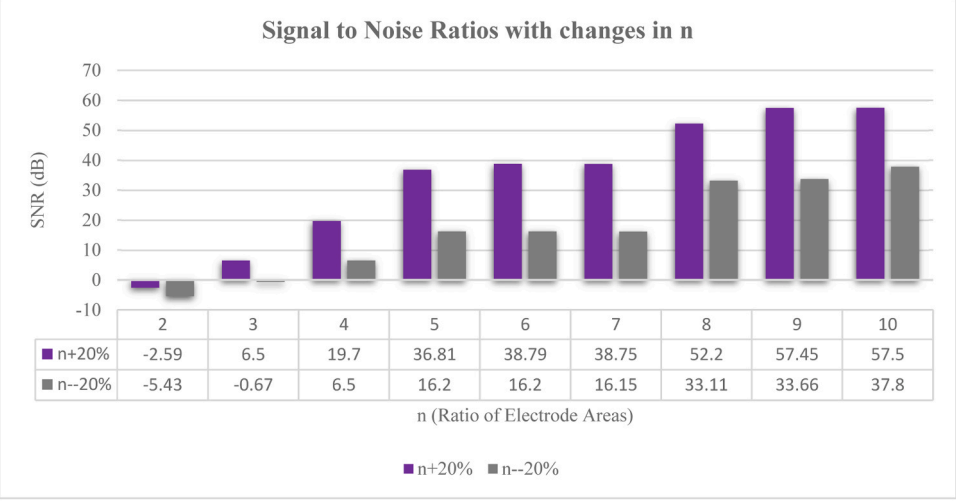

Fig. 15. Signal Noise Ratios with changes in n.

CRediT authorship contribution statement

Kalra Anubha Manju: Conceptualization, Data curation, Methodology, Writing – original draft. **Anand Gautam:** Data curation, Writing – original draft, Writing – review & editing. **Lowe Andrew:** Investigation, Supervision, Visualization. **Simpkin Ray:** Validation, Writing – review & editing. **Budgett David:** Writing – review & editing.

Declaration of Competing Interest

The authors declare that they have no known competing financial interests or personal relationships that could have appeared to influence the work reported in this paper.

Data availability

Data will be made available on request.

Acknowledgements

The authors would like to express their sincere gratitude to Ministry of Business, Innovation and Employment for the financial support provided under Smart Ideas Grant titled “Smart Biopotential Sensors, 2016” We also appreciate both Institute of Biomedical Technologies and School of Engineering, Computing and Mathematical Sciences at Auckland University of Technology for their contribution to fund for Electrical/ Mechanical components and Printed Circuit Boards required for pilot testing. The resources and facilities provided by them were instrumental in the successful completion of this study.

Appendix A. Supporting information

Supplementary data associated with this article can be found in the online version at doi:10.1016/j.sna.2023.114989.

References

[1] E. Fung, et al., Electrocardiographic patch devices and contemporary wireless cardiac monitoring, Front. Physiol. 6 (2015), https://doi.org/10.3389/fphys.2015.00149.
[2] H.L. Kennedy, The history, science, and innovation of Holter technology, Ann. Noninvasive Electrocardiol. 11 (1) (2006) 85–94, https://doi.org/10.1111/j.1542-474X.2006.00067.x.
[3] K.E. Sandau, et al., Update to practice standards for electrocardiographic monitoring in hospital settings: a scientific statement from the American Heart Association, Circulation 136 (19) (2017) e273–e344, https://doi.org/10.1161/CIR.0000000000000527.
[4] ‘Rosenberg: Use of a Noninvasive Continuous Monitoring. - Google Scholar [Online]. ⟨https://scholar.google.com/scholar_lookup?title=Use%20of%20a%20noninvasive%20continuous%20monitoring%20device%20in%20the%20management%20of%20atrial%20fibrillation%3A%20a%20pilot%20study&journal=Pacing%20Clin%20Electrophysiol&doi=10.1111%2Fpace.12053&volume=36&pages=328–333&publication_year=2013&author=Rosenberg%2CMA&author=Samuel%2CM&author=Thosani%2CA&author=Zimetbaum%2CPJ⟩. (Accessed 22 March 2023.
[5] A. Zompanti, et al., Development and test of a portable ECG device with dry capacitive electrodes and driven right leg circuit, Sensors 21 (8) (2021) 8, https://doi.org/10.3390/s21082777.
[6] S. Ramasamy, A. Balan, Wearable sensors for ECG measurement: a review, Sens. Rev. 38 (4) (2018) 412–419, https://doi.org/10.1108/SR-06-2017-0110.
[7] T.-W. Wang, S.-F. Lin, Non-contact capacitive sensing for ECG recording in small animals, Meas. Sci. Technol. 31 (12) (2020) 125703, https://doi.org/10.1088/1361-6501/ab8cfc.
[8] S.-H. Liu, Motion artifact reduction in electrocardiogram using adaptive filter, J. Med. Biol. Eng. 31 (1) (2011) 67–72.
[9] S.W. Yoon, S.D. Min, Y.H. Yun, S. Lee, M. Lee, Adaptive motion artifacts reduction using 3-axis accelerometer in e-textile ECG measurement system, J. Med. Syst. 32 (2008) 101–106.
[10] M.A.D. Raya , L.G. Sison, Adaptive noise cancelling of motion artifact in stress ECG signals using accelerometer, in: Proceedings of the Second Joint Twenty Fourth Annual Conference and the Annual Fall Meeting of the Biomedical Engineering Society][Engineering in Medicine and Biology, IEEE, 2002, 1756–1757.
[11] T.-H. Kang, Textile-embedded Sensors for Wearable Physiological Monitoring Systems, 2007.
[12] G. Peng, A Non-contact, Low-noise Electrocardiogram Sensor ASIC Employing Motion Artifact Reduction, University of Rochester, 2014.
[13] A. Yilmaz, O. Javed, M. Shah, Object tracking: a survey, ACM Comput. Surv. (CSUR) 38 (4) (2006) 13-es.
[14] N.V. Thakor, Y.-S. Zhu, Applications of adaptive filtering to ECG analysis: noise cancellation and arrhythmia detection, IEEE Trans. Biomed. Eng. 38 (8) (1991) 785–794.
[15] C.K. Chui, An Introduction to Wavelets, 1, Academic Press, 1992.
[16] A.N. Akansu, W.A. Serdijn, I.W. Selesnick, Emerging applications of wavelets: A review, Phys’. Comm, 2010.
[17] Ho Tatt Wei, V. Jeoti, A wavelet footprints-based compression scheme for ECG signals, IEEE (2004) 283–286, https://doi.org/10.1109/TENCON.2004.1414412.
[18] S. Kim et al., Influence of contact pressure and moisture on the signal quality of a newly developed textile ECG sensor shirt, in: Proceedings of the Fifth International Summer School and Symposium on Medical Devices and Biosensors, IEEE, 2008, 256–259.
[19] A. Cömert, M. Honkala, J. Hyttinen, Effect of pressure and padding on motion artifact of textile electrodes, Biomed. Eng. Online 12 (2013) 1–18.
[20] J. Ding, Y. Tang, R. Chang, Y. Li, L. Zhang, F. Yan, Reduction in the motion artifacts in noncontact ECG measurements using a novel designed electrode structure, Sensors 23 (2) (2023) 2, https://doi.org/10.3390/s23020956.
[21] ‘US Patent Application for a biopotential sensor, device and process, Patent Application (Application #20220202336 issued June 30, 2022) - Justia Patents Search’ [Online]. ⟨https://patents.justia.com/patent/20220202336⟩. (Accessed 22 March 2023).
[22] ‘A review of textile-based electrodes developed for electrostimulation - Luisa Euler, Li Guo, Nils-Krister Persson, 2022′ [Online]. ⟨https://journals.sagepub.com/doi/10.1177/00405175211051949⟩. (Accessed 22 March 2023).
[23] W. Chang, et al., Fibril-type textile electrodes enabling extremely high areal capacity through pseudocapacitive electroplating onto chalcogenide nanoparticle-encapsulated fibrils, Adv. Sci. 9 (33) (2022) 2203800, https://doi.org/10.1002/advs.202203800.
[24] ‘How to Calculate a Capacitance Matrix in COMSOL Multiphysics®, COMSOL [Online]. ⟨https://www.comsol.com/blogs/how-to-calculate-a-capacitance-matrix-in-comsol-multiphysics/⟩. (Accessed 28 November 2023).

Anubha Manju Kalra is a lecturer in the Electrical and Electronics department at Auckland University of Technology (AUT). She was previously a research fellow in biomedical engineering at the Institute of Biomedical Technologies, Auckland University of Technology (AUT), New Zealand. Currently working on the EXGware research, approved by the Ministry of Business, Innovation, and Education. The research team comprises researchers, scientists, and doctors -from AUT Rehabilitation, University of Auckland, Callaghan Innovation, New Zealand Brain Research Institute, and industrial partners -Noxatec, Exsurgo Rehab, Fisher and Paykel Healthcare, and Electronic partners.

Gautam Anand completed his Ph.D. in Biomedical Engineering from AUT in 2017 to add to his M.Eng.St. degree from AUT in 2013 and B.Tech (Hons) in 2012 from India. His research interests focus on biomedical engineering, specifically designing sensor systems for monitoring biopotentials such as ECG and bioimpedance. He is involved in wearable sensing, sensor simulation and design, data acquisition and processing, mathematical modelling, hemodynamic assessment, dielectric properties of biomaterials and ambulatory patient monitoring.

Andrew Lowe is currently Professor in Mechanical Engineering, and Director of the Institute of Biomedical Technologies at Auckland University of Technology. His current research activities are directed towards measurement and modelling of the cardiovascular system in order to improve cardiovascular risk management in primary and community care and advancing measurement of electrical signals generated by the human body.

Ray Simpkin Highly experienced research scientist and engineer with a demonstrated history of working in the public and private sector R&D space for over 40 years. Skilled in Electromagnetics, Microwave Engineering, Mathematical Modeling, Long-range Wireless Power Transfer, Materials Science, Medical Devices, Spectroscopy, and Project Management. Strong research professional with a Bachelors degree in Physics (BSc - 1st class hons) and Doctor of Philosophy (Ph.D.) in Electromagnetics, both acquired from Imperial College London. In 2020, he received a Lifetime Achievement Award from Science New Zealand.

David Budgett has a Ph.D. in Electrical Engineering from Imperial College in London. He graduated with BE in Electrical Engineering from the University of Canterbury. He has held lecturing positions in the Department of Engineering Science, the University of Auckland, and the School of Engineering, University of Sussex. David has a long history of developing implantable devices and has been involved in multiple startup companies originating from the Auckland Bioengineering Institute. He has a special interest in promotion of pelvic floor health and is the CTO with JUNOFEM.